NASA/TM-20205010032

High Ice Water Content Associated with a Darwin, Australia, Mesoscale Convective System

Fred H. Proctor
Distinguished Research Associate
Langley Research Center, Hampton, Virginia

George F. Switzer
Analytical Mechanics Associates, Inc., Hampton, Virginia

November 2020

NASA STI Program . . . in Profile

Since its founding, NASA has been dedicated to the advancement of aeronautics and space science. The NASA scientific and technical information (STI) program plays a key part in helping NASA maintain this important role.

The NASA STI program operates under the auspices of the Agency Chief Information Officer. It collects, organizes, provides for archiving, and disseminates NASA's STI. The NASA STI program provides access to the NTRS Registered and its public interface, the NASA Technical Reports Server, thus providing one of the largest collections of aeronautical and space science STI in the world. Results are published in both non-NASA channels and by NASA in the NASA STI Report Series, which includes the following report types:

- TECHNICAL PUBLICATION. Reports of completed research or a major significant phase of research that present the results of NASA Programs and include extensive data or theoretical analysis. Includes compilations of significant scientific and technical data and information deemed to be of continuing reference value. NASA counter-part of peer-reviewed formal professional papers but has less stringent limitations on manuscript length and extent of graphic presentations.

- TECHNICAL MEMORANDUM. Scientific and technical findings that are preliminary or of specialized interest, e.g., quick release reports, working papers, and bibliographies that contain minimal annotation. Does not contain extensive analysis.

- CONTRACTOR REPORT. Scientific and technical findings by NASA-sponsored contractors and grantees.

- CONFERENCE PUBLICATION. Collected papers from scientific and technical conferences, symposia, seminars, or other meetings sponsored or co-sponsored by NASA.

- SPECIAL PUBLICATION. Scientific, technical, or historical information from NASA programs, projects, and missions, often concerned with subjects having substantial public interest.

- TECHNICAL TRANSLATION. English-language translations of foreign scientific and technical material pertinent to NASA's mission.

Specialized services also include organizing and publishing research results, distributing specialized research announcements and feeds, providing information desk and personal search support, and enabling data exchange services.

For more information about the NASA STI program, see the following:

- Access the NASA STI program home page at http://www.sti.nasa.gov

- E-mail your question to help@sti.nasa.gov

- Phone the NASA STI Information Desk at 757-864-9658

- Write to:
  NASA STI Information Desk
  Mail Stop 148
  NASA Langley Research Center
  Hampton, VA 23681-2199

NASA/TM-20205010032

High Ice Water Content Associated with a Darwin, Australia, Mesoscale Convective System

Fred H. Proctor
Distinguished Research Associate
Langley Research Center, Hampton, Virginia

George F. Switzer
Analytical Mechanics Associates, Inc., Hampton, Virginia

National Aeronautics and
Space Administration

Langley Research Center
Hampton, VA 23681

November 2020

Abstract

A mesoscale convective complex that occurred during the 2014 Darwin, Australia, flight campaign is examined via a three-dimensional, numerical simulation. The focus of the study is to better understand the presence and development of High Ice Water Content (HIWC) that was observed in the actual storm. Although peak values of ice water content may occur early in the storm lifetime, large areas of high concentrations expand with time and persist even when the storm tops begin to warm. The storm canopy which contains HIWC, has low radar reflectivity factor and is fed by an ensemble of regenerating thermal plumes. Detection via weather radar of the aviation hazard associated HIWC is challenging due the low values of radar reflectivity factor.

Acknowledgments

This research is sponsored by the Advanced Air Transport Technology Project of NASA's Advanced Air Vehicles Program. The authors would like to acknowledge the contributing organizations that enabled the HAIC-HIWC Darwin Flight Campaign. These are: the European Union's Seventh Framework Program in research, technological development and demonstration under grant agreement ACP2-GA-2012-314314, the European Aviation Safety Agency (EASA) Research Program under service contract EASA.2013.FC27, the FAA Aviation Research Division and Aviation Weather Division, the NASA Aviation Safety Program, the Boeing Company, and Transport Canada. Additional support to this campaign was provided by Met Analytics, Science Engineering Associates, the Australian Bureau of Meteorology, Environment Canada, the National Research Council of Canada, the National Center for Atmospheric Research, Airbus SAS Operations, Centre National de la Recherche Scientifique (CNRS), and the Service des Avions Français Instrumentés pour la Recherche en Environnement (SAFIRE). The authors also would like to thank Steven Harrah (NASA Langley Research Center), Tom Ratvasky (NASA Glenn Research Center), and Walter Strapp (Met Analytics) for their programmatic, technical, and operational support; and the NASA Langley Satellite Group for providing satellite images. The numerical simulations were conducted using the Pleiades high-performance supercomputer cluster of the NASA Advanced Supercomputing Division. An earlier version of this paper was presented in: Proctor, F.H., and Switzer, G.F., "Numerical Simulation of HIWC Conditions with the Terminal Area Simulation System," AIAA-2016-4203, doi: 10.2514/6.2016-4203.

Nomenclature

dBZ	=	decibels of radar reflectivity factor Z (decibels of mm^6 m^{-3})
D_{ic}	=	ice crystal diameter (*m*)
D_R	=	raindrop diameter
D_S	=	snow particle diameter
g	=	acceleration due to earth's gravity
$\|K_I\|^2$	=	dielectric factor for ice (=0.21)
$\|K_W\|^2$	=	dielectric factor for water (=0.93)
HAIC	=	High Altitude Ice Crystals
HIWC	=	High Ice Water Content (IWC > 1 $g\ m^{-3}$)
IMC	=	Instrumented Meteorological Conditions
IWC	=	ice water concentration (g/m^3)
M_R	=	mass water content for rain ($g\ m^{-3}$)
$N(D_R)$	=	number of raindrops per unit diameter D_R per unit volume
$N(D_S)$	=	number of snow particles per unit diameter D_S per unit volume
N_{oH}	=	intercept value in hail/graupel particle size distribution (m^{-4})
t	=	time coordinate
TASS	=	Terminal Area Simulation System
T_C	=	temperature (Centigrade)
x,y	=	orthogonal space coordinates in lateral plane
V	=	horizontal component of velocity in y direction
z	=	vertical coordinate, elevation
Z_R	=	radar reflectivity factor from rain
Z_S	=	radar reflectivity factor from snow
δ_S	=	snow particle density
δ_W	=	specific density of water

I. Introduction

High concentrations of ice crystals associated with the upper-regions of large convective systems pose a threat to the safety of commuter and large-transport jet aircraft. The ingestion of high concentrations of ice crystals can cause uncommanded jet-engine power loss, such as roll-back and unstart, and in some cases result in engine damage.[1] The threat regions consist entirely, if not primarily, of ice crystals and differ from icing that is caused by accretion of supercooled water drops. In fact, reports of ice accretion during these events are rare.[2] These regions of dense ice-crystal concentrations are typically referred to as either High Ice Water Content[3] (HIWC) or High Altitude Ice Crystals[4,5,6] (HAIC), and have been linked with over a hundred and seventy incidents.[7] These incidents continue to occur with an average of about ten such incidents a year. Pilots have been able to restart engines or gain lost power once they have descended into warmer regions or have moved outside the threat area, and the primary impact of the incidents being financial in the form of engine replacement and downtime for aircraft inspections.

Large areas of ice crystals that expose jet engines for a duration of time (i.e. several minutes or more) seem more of a factor than brief encounters with local areas that have high concentrations. Thus, the HIWC threat is most associated with the large canopies of mesoscale convective systems,[8] rather than chance encounters with isolated short-lived thunderstorms. Detection of HIWC with the aircraft's weather radar is challenging, since the HIWC regions usually have low radar reflectivity factor and appear innocuous. In some cases HIWC incidents have occurred with only "black" (i.e. < 20 dBZ) being displayed from the aircraft's weather radar, although higher reflectivity may be detected at elevations below the event. According to Grzych and Mason,[9] satellites have detected a significant cold cloud-top region overlaying the location of most engine events. Other observations that may be associated with HIWC incidents include: presence of light turbulence (but rarely exceeding moderate), poor visibility (IMC), heavy rain below the freezing level, precipitation impacting the windshield, an indicated warming of the total air temperature (TAT) due to restrictions from accumulated ice in the TAT probe, St Elmo's fire, absence of hail, and cloud canopies that bulge above the tropopause. Environmental weather conditions leading to storms favorable for generating HIWC events are similar to those that produce mesoscale convective systems and tropical storms. Only a few HIWC incidents have been reported with supercell convection, perhaps due to their association with higher levels of radar reflectivity factor that aircraft routinely detect and avoid. Most aircraft incidents have occurred from systems forming in deep moist environments with moderate to low convective instability.[9] Tropical and oceanic mesoscale convective systems are likely candidates for producing HIWC events due to their large size and persistence.[10] The environment needed to produce these type systems, have deep levels of moisture and a moderate convective instability.

Another threat from HIWC is that large concentrations of ice crystals can cause blockage or restriction of the aircraft Pitot tubes, resulting in a loss of important information that may be critical for flight systems and pilot control. During NASA's DC-8 flight test in August of 2015, Pitot tube anomalies occurred in six of ten flights,[11] when HIWC was encountered and air temperatures were colder than -29C (see Fig. 1).

In order to better understand the characteristics of a HIWC event, a numerical simulation with a cloud-scale weather model is utilized. The case chosen for this simulation is an event from the International HAIC-HIWC Darwin 2014 Field Campaign[12] that was conducted at Darwin, Australia in the winter of 2014.[5,13] Observations from this case are briefly described in Section II, followed by a description of the model and initial conditions in sections III and IV, and followed by an analysis of the simulation in section V. This case is selected because it is believed typical of an oceanic HIWC system and has the availability of relatively good measurements.

Figure 1. Ice accumulation on TAT (left) and Pitot tube (right) sensors during encounter with HIWC conditions. Photographs taken from DC-8's cockpit during NASA's 2015 HIWC flight campaign.

II. Darwin 23 January 2014 Case

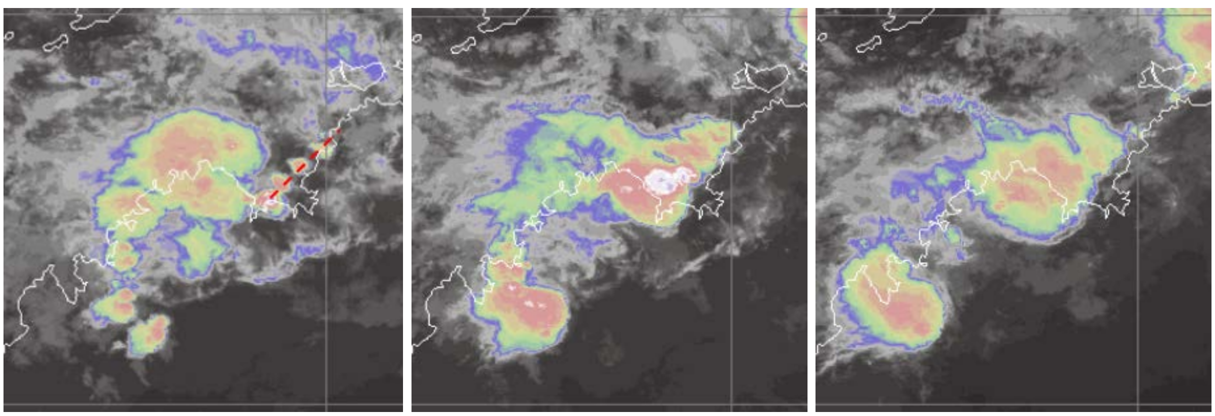

1830 UTC 2010 UTC 2240 UTC

Figure 2. Infrared satellite imagery showing cloud top temperatures of a mesoscale convective system offshore of Northern Australia on 23 January 2014. Lat/Long of window is 122ºE-132ºE, 10ºS-20ºS. At 1830 UTC, the line of developing convection (indicated by dashed line in left most figure) is located just to the east of a dying convective system. Imagery courtsey of P. Minnis and L. Nguyen, NASA Langley Satellite Team.

Off the coast of Northwestern Australia, about 200 *km* southwest of Darwin, a line of convection developed nearly parallel to the coast. This convection appeared to be triggered by an old outflow boundary from previous existing convection. A southwest-northeast line of at least four distinct cloud tops reached tropopause levels and began to expand in scale as shown in Fig. 2. The convection initially was spaced about 50 *km* apart. The cloud anvils above the distinct convective systems soon merged and spread to the northwest. Coldest cloud tops were achieved several hours after convention began. The system appeared to weaken as indicated by warmer cloud tops, some 4 to 5 hours after its initial appearance. Visible satellite imagery that became available following sunrise (Fig. 3), indicated a near-stationary line, with a weak propagation toward the southeast.

An instrumented research aircraft probed the system with multiple passes at flight levels between 2100 UTC and 2300 UTC. The aircraft was equipped with an IsoKinetic Probe (IKP)[14] which measured extended ice water concentrations (IWC) greater than 1 $g\ m^{-3}$ and peak values exceeding 3 $g\ m^{-3}$. The highest concentrations were measured during the last pass of the flight, with IWC above 2 $g\ m^{-3}$ persisting for three minutes and above 1 $g\ m^{-3}$ for five minutes.

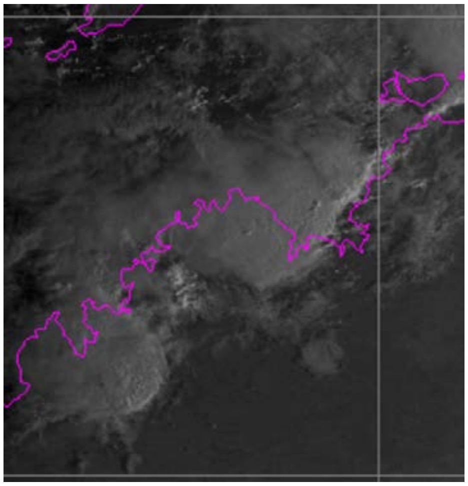

Figure 3. Same as in Fig. 2, but for visible satellite imagery at 2210 UTC. Courtesy of P. Minnis and L. Nguyen, NASA Langley Satellite Team.

Unfortunately, ground-based weather radar was located too far away to provide useful data of this system.

This mesoscale convective system seems to typify many past events associated with HIWC. Because the deep convective system persisted for several hours, large cloud canopies formed and expand with time.

III. Model Description

The numerical simulation is performed with NASA's Terminal Areas Simulation System (TASS) which has the capability of simulating both liquid- and ice-phase cloud processes.[15,16,17,18,19] The TASS model is three dimensional, and has prognostic equations for momentum, potential temperature, and pressure, as well as prognostic equations for continuity of water substance. The lateral boundaries can be open or cyclic.

For treating cloud growth and precipitation development, TASS has over 60 bulk cloud microphysical submodels similar to those used by Lin et al.,[20] and Rutledge and Hobbs.[21] The autoconversion of cloud droplets into rain is based on drop growth studies by Berry and Reinhardt,[22,23] and allows for differences in droplet size between continental and maritime locations.[15] Rain is assumed to have an inverse-exponential drop distribution with an intercept that increases with rainwater concentration.[24]

TASS divides the prediction of ice particles into three different categories: 1) ice crystal water — which represents small hexagonal ice crystals, 2) Snow — which represents larger precipitating ice particles, and 3) graupel (or hail) — which represents even larger more dense particles that are produced from freezing rain drops and riming snow particles. The ice crystal water is assumed to have a monodispersed particle size that is limited to diameters of about 200 μm. The snow water assumes particles with an inverse exponential distribution that has an intercept that increases with decreasing temperature.[25] Hence, at colder temperatures, the assumed distributions will have smaller particles than at warmer temperatures. The graupel particles also assume an inverse exponential distribution, but with a smaller intercept and a larger particle density than snow. Several of the key parameters assumed for the particle distributions are shown in Table 1.

Radar reflectivity factor is diagnosed from TASS based on the predicted water content and assumed particle distributions. The approach assumes Rayleigh scattering and is based on Smith et al.[26] For example, the radar reflectivity factor for rain based on Rayleigh scattering is:

$$\boldsymbol{Z_R} = \int_{\mathbf{0}}^{\infty} \boldsymbol{N}(\boldsymbol{D_R})\, \boldsymbol{D_R^6 dD_R}$$

The radar reflectivity factor for ice particles consider the dielectric factors for ice and water and depend upon whether the particle is undergoing either wet or dry growth. For example the contribution to radar reflectivity factor for “dry” snow adjust for the melted diameters is:

$$\boldsymbol{Z_S} = \frac{|\boldsymbol{K_I}|^2}{|\boldsymbol{K_W}|^2}\ \frac{\boldsymbol{\delta_S^2}}{\boldsymbol{\delta_w^2}} \int_{\mathbf{0}}^{\infty} \boldsymbol{N}(\boldsymbol{D_S})\, \boldsymbol{D_S^6 dD_S}$$

Some discrepancy between simulated and observed radar reflectivity factor is expected, since the above method does not take into account the radar beam size, geometry, attenuation, refraction, and ground clutter.

The TASS model equations are discretized using quadratic-conservative fourth-order finite-differences in space for the calculation of momentum and pressure fields,[27] and the third-order upstream-biased Leonard scheme[28] is used to calculate the transport of potential temperature and water vapor. A Monotone Upstream-centered Scheme for Conservation Laws (MUSCL)-type scheme after van Leer[29,30] is used for the transport of water substance variables. The Klemp-Wilhelmson time-splitting scheme[31] is used for computational efficiency, in which the higher-frequency terms are integrated by enforcing the CFL criteria to take into account sound wave propagation due to compressibility effects. The remaining terms are integrated using a larger time step that would be appropriate for anelastic and incompressible flows.[32] The Adams-Bashforth scheme is assumed for time differencing of momentum and pressure for both large and small time step approximations. The TASS model is programmed in FORTRAN and operates efficiently on massively-parallel computer architectures using Message Passing Interface (MPI) library calls.

Table 1 ***Key parameters and relationships in TASS microphysics.***

Category	Size Distribution Intercept m^{-4}	Particle Density $kg\ m^{-3}$	Comment
Liquid Cloud Water	**Monodispersed**	**50**	**Number of droplets per volume is an input**
Rain	**Inverse exponential** $N_0 = 7.106 \times 10^6\ M_R^{0.648}$	**1000**	**Intercept increases with rainwater content,** M_R **(g** m^{-3}**)**
Cloud Ice	**Monodispersed**	**Particle mass (kg) =** $0.1758\ D_{ic}^{2.2}$	**Hexagonal plates Diameter mostly < 200 µm**
Snow	**Inverse exponential** $N_0 = 10^{(6.7 - 0.03\ Tc + \Psi)}$, **where** $\Psi = 1.45\ M_s - 0.375\ M_s^2 - 0.005\ M_s^3$ **for** $M_s < 3.5$ **g** m^{-3} **and** $4^oC > Tc > -55^oC$	**100 if** $Tc < -15^oC$ **or** $100[1+(Tc+15)/15]$ **if** $0 > Tc > -15^oC$	**Intercept increases with decreasing temperature and increasing snow concentration,** M_s **(g** m^{-3}**)**
Hail/Graupel	**Inverse exponential Intercept is an input parameter**	**Either 450 if graupel or 800 if hail**	**Intercept decreases with temperature below melting level**

Initiation packages are available for triggering convective systems, turbulence, and aircraft wake vortices. TASS has a rich history of application to weather and wake vortex phenomenology,[33,34] and has supported other NASA projects for the past 35 years.[35] Table 2 lists the salient characteristics of TASS.

Simulations with TASS have been used to 1) investigate and characterize regions of HIWC, 2) provide numerical data sets that can be used with radar simulation tools, and 3) contribute to the development of radar software for detecting regions of HIWC and other aviation hazards.

Table 2 Salient Features in TASS

• **Ambient conditions initialized with atmospheric sounding**
• **Arakawa C-grid staggered numerical mesh**
• **Bulk parametrizations for cloud microphysics (over 60 sub-models)**
• **Compressible, time-split formulation**
• **Efficient and accurate conservative numerical schemes with 4th order accuracy in space**
• **Ground or Ocean boundary condition with surface-stress based on Monin Obukhov Similarity Theory**
• **History of application to aviation weather and safety problems**
• **Initialization packages for: convective storms, microbursts, turbulence, planetary boundary layer, tropical cyclones, and aircraft wake vortices**
• **Large Eddy Simulation with subgrid scale turbulence closure**
• **Liquid, vapor, and ice phase microphysics**
• **Meteorological framework**
• **Model simulations validated with field data and theoretical solutions**
• **Monotone upstream-centered schemes for water substance**
• **NonBousssinesq equation set**
• **Nonreflective boundary conditions for open boundaries**
• **Option of either open or periodic lateral boundaries**
• **Option of either periodic or impermeable top and bottom boundaries**
• **Prognostic equations for velocity, pressure, potential temperature, dust/insects, and water substance**
• **Scales efficiently with multiple processors as used on high-performance supercomputer clusters using the Message Passing Interface (MPI) library**
• **Storm-tracking, movable grid domain**
• **Variable time step to ensure CFL criteria for numerical stability**
• **Vreman subgrid turbulence closure model with modification for stratification and flow rotation**
• **Water substance represented by water vapor, liquid cloud water, rain, cloud ice, snow, and hail/graupel**
• **Wet and dry growth for hail and snow**

IV. Model Configuration and Initialization

A single sounding is used to initialize the simulation. The rawinsonde sounding nearest to the time and location of the convective event was observed for Darwin at 0000 UTC on 24 January 2014. Since the convective event develops several hours earlier and is approximately 200 *km* to the southwest, the observed sounding is modified to be consistent with the observed surface temperature in the vicinity of the event, and is moistened through a deep layer as is frequently found in the environment of HIWC systems.[9] The modified sounding is shown in Fig. 4.[36] It has moderate convective instability, with a windshear vector between cloud base and 6-*km* elevation that is directed from 75^o (east-northeast). The sounding's tropopause height and temperature are 15.55 *km* and -76.8^{o}C, respectively. The melting level is at an altitude of 5.2 *km*.

In order to achieve sufficient resolution needed for important convective scales, while retaining an adequately large domain, the physical domain size is configured as 45 *km* wide x 112.5 *km* long. In addition, cyclic boundary conditions are assumed for the left and right boundaries; and the domain is rotated 15° in the counter-clockwise direction so that the low-level shear vector aligns orthogonal to the cyclic boundaries. The vertical depth of the domain is ~18.6 *km*. The computational domain is defined by 304x753x128 grid points with a grid size of 150 *m* in each direction.

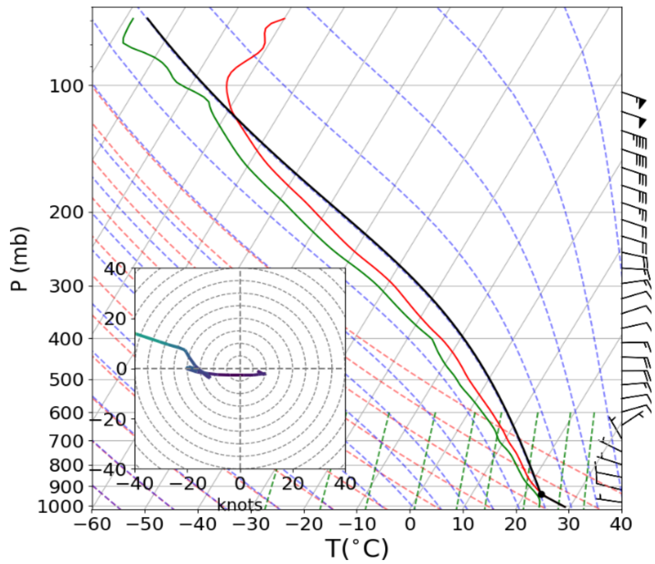

Figure 4. Skew-T environmental sounding for Darwin case. Modified from sounding observed at Darwin Australia, at 0000 UTC, 24 January 2014. Wind hodograph inserted.

The ground surface is assumed flat and represents the ocean surface. Coastlines and topographical features are not incorporated into the simulation. Maritime cloud droplet concentrations are assumed as 75 droplets cm^{-3}, and the graupel intercept is set at 4 x 10^5 m^{-4}.

V. Results

The simulation is initialized with a thermal impulse and is integrated in time for 270 min (four and a half hours). Convection is triggered and orients itself along a nearly stationary gust front. The anvils of the convective cells fuse into a cloud canopy which expands northwestward similar to the observations described in in section II. The simulated convective system is long lived, although it begins to weaken shortly before four hours. An ensemble of regenerating updraft plumes, mostly originating along the forward line of the system, create ice particles that feed into the expanding upper-level canopy (Fig. 5).

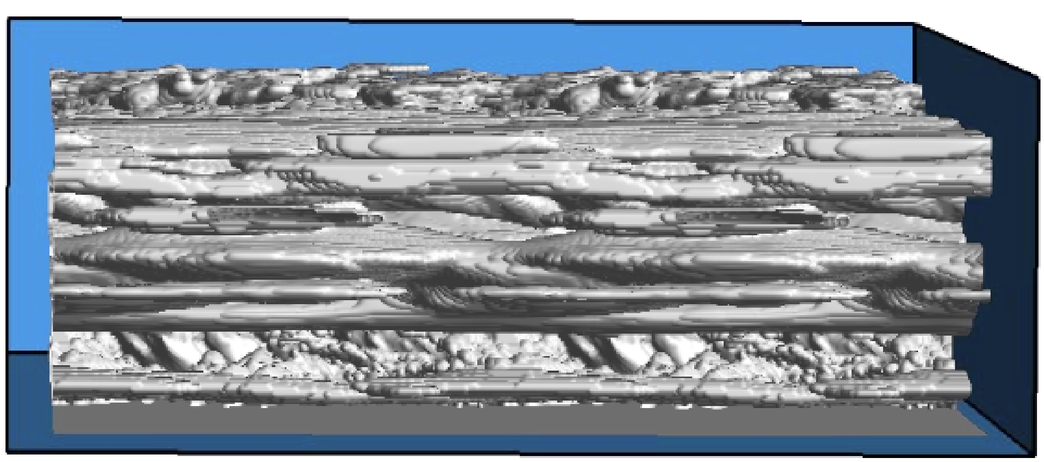

Figure 5. View of simulated three dimensional convective system from south (at t = 210 min). Numerous cumulus plumes are evident along the forward edge of the system. From three-dimensional rendering of cloud and precipitation surfaces with vertical dimension exaggerated.

A comparison of model and available observed data for the Darwin case is summarized in Table 3. The model simulation appears to catch the basic features of the storm, although the horizontal scale of the highest concentrations of ice is underpredicted. Also, there is slight difference in orientation of the convective line, which could be due to environmental difference not represented by the initial sounding.

Table 3. Comparison between observed and simulated features for the Darwin case.

Parameter	Observed	TASS
Orientation of convective line	southwest to northeast	west-southwest to east-northeast
Lifetime of system	5+ hours	4+ hours
Coldest cloud top temperature	-87ºC at 2019 UTC	-86ºC at t =165 minutes
Primary direction of canopy expansion	toward west-northwest	toward northwest
Line movement	nearly stationary	nearly stationary
Maximum IWC at flight level	3.5 $g\ m^{-3}$	3.5 $g\ m^{-3}$
Maximum scale of IWC greater than 1 $g\ m^{-3}$	65 *km*	40 *km*
Maximum scale of IWC greater than 2 $g\ m^{-3}$	40 *km*	10 *km*

A. Evolution of Simulated Fields

The tops of the convective system first reach the tropopause around 85 *min* into the simulation. Overall peaks reach an elevation of 17.5 *km* at 120 *min*. Precipitation cooled outflows near the surface help regenerate other updraft plumes located along a forward line of heavy rain. Lighter rain spreads northwestward behind the line, with a few convective plumes developing under the canopy along the northwestern edge of the precipitation. The intensity of the system slowly weakens after 160 *min*, although convection remains vigorous and the system continues to expand in scale.

The maximum ice water concentration above an elevation of 9 *km* is shown in Fig. 6. Peak values of over 3.5 $g\ m^{-3}$ are achieved early in the system's lifetime; but during the early stages, graupel contributes to a portion of the overall ice content. With time, the ice water concentrations expand in area and consist almost entirely of snow and cloud ice. As indicated in Fig. 6, peak IWC remains at or above 3 $g\ m^{-3}$ until 205 min (3 hrs, 25 min) into the simulation. After which, they begin to drop off. These values for IWC are similar to what NASA has encountered in its HIWC flight campaigns.[37] In a review of deep-convective microphysics studies, Lawson et al.[2] reports measurements of IWC of up to 2.5 $g\ m^{-3}$. Peak values in excess of 3 $g\ m^{-3}$ have been measured during recent HIWC and HAIC flight campaigns.[11]

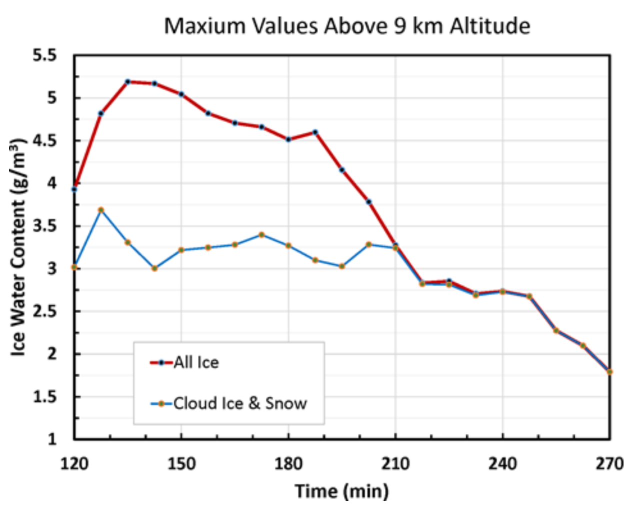

Figure 6. Maximum ice water concentration above 9 km vs simulation time. The curve for "all ice" includes the contribution from graupel, as well as ice crystals and snow.

The evolution of the storm is arbitrarily broken into four stages with times referenced to the initiation of this simulation. The early stage (~120 *min*) when the storm is rapidly growing in size and intensity, but storm canopies cover a relatively small area; the intense stage (~165 *min*) when large IWC occur, and the area of HIWC is rapidly increasing; the mature stage (~210 *min*) when large areas of HIWC have been achieved; and the decay stage (~232 *min*) when the storm weakens and IWC decreases.

Time evolution of the cloud top temperatures, as well as the radar reflectivity factor and cloud ice water fields across three of these stages are shown in Fig. 7. Horizontal cross-sections at 10 *km* elevation are chosen since it will be near flight level and little or no liquid water is expected since temperatures are colder than -30^{o}C. Three different times are chosen from the simulation. The first column is at t = 120 *min* (2*hr*) and represents the early stage when the cloud tops are beginning to coalesce and fuse into a rapidly expanding canopy. The second column is at t = 165 *min* (2*hr*: 45 *min*) representing the intense stage, when cloud tops are very cold and when peak IWC are large and beginning to expand over a significant area. The third column is at t = 232.5 *min* (3*hr*: 52.5 *min*), represents the decay stage. At this last stage the cloud tops are extensive, but have become warmer (lower in elevation) and peak IWC have noticeably decreased. At this altitude, only small areas of green (23 dBZ - 33 dBZ) are shown for the radar reflectivity factor during the first two stages, and no green (or higher) is evident at the last stage. Since most airborne weather radars would not display reflectivity factor below intensities indicated by green, then most of the area within the cloud canopy would appear innocuous as viewed from an airborne weather radar display (especially during the mature stage). These weak values of radar reflectivity factor at flight level are consistent with those found for deep oceanic convection by Heymsfield et al.[38] and during NASA's 2015 HIWC flight campaign. It is important to note from Fig. 7, that the highest IWC correlates with the locations of the overshooting tops and peak radar reflectivity factor during the early period of the storm system, but the coldest tops begin to warm and are displaced downshear from the regions of higher IWC as the storm matures.

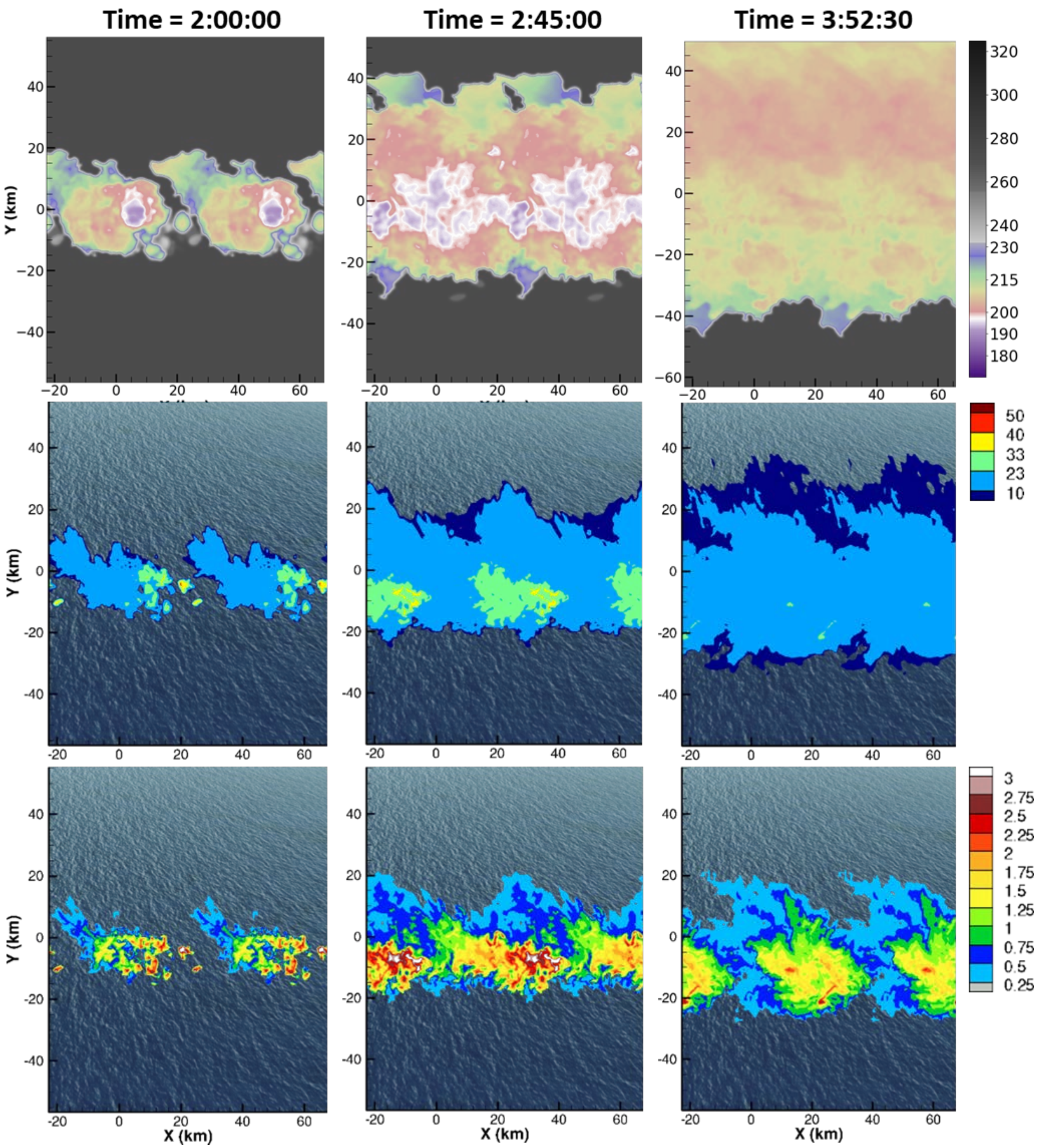

Figure 7. Horizontal cross-sections of evolving fields at three different times from TASS. The same color scale for cloud top temperature in Kelvin (top row) as in Fig. 2 for the observed satellite imagery. The second row is radar reflectivity factor at 10 km elevation, and the third row is ice water concentration g m-3, also at z = 10 km. The first column is at t = 120 min (early stage), the second column is at t = 165 min (intense stage), and the third column is at t = 232.5 min during decay stage. Coordinates relative to initial model grid with y directed toward NNE.

Vertical cross-sections of radar reflectivity factor taken orthogonal to the convective line are shown at both the intense and decay stages in Fig. 8. Highest radar reflectivity factor is found near the melting level (z = 5.2 km) and also near the surface. Above the melting level, the radar reflectivity factor decreases with increasing elevation. This is consistent with radar measurements of deep oceanic convection, as reported in Heymsfield et al.[38] Near the ground, heavy showers fall beneath the developing storm; and later in time, evolve into a large area of steady rain. This widespread area of rain is produced from melting snow falling from the upper- and mid-levels of the expanding storm. Again, radar reflectivity factor can be relatively weak in regions of HIWC, and high values of radar reflectivity factor may not always be found directly beneath regions of high IWC. The highest IWC occurs near the forward area of the convective line, where convective plumes continue to be regenerated.

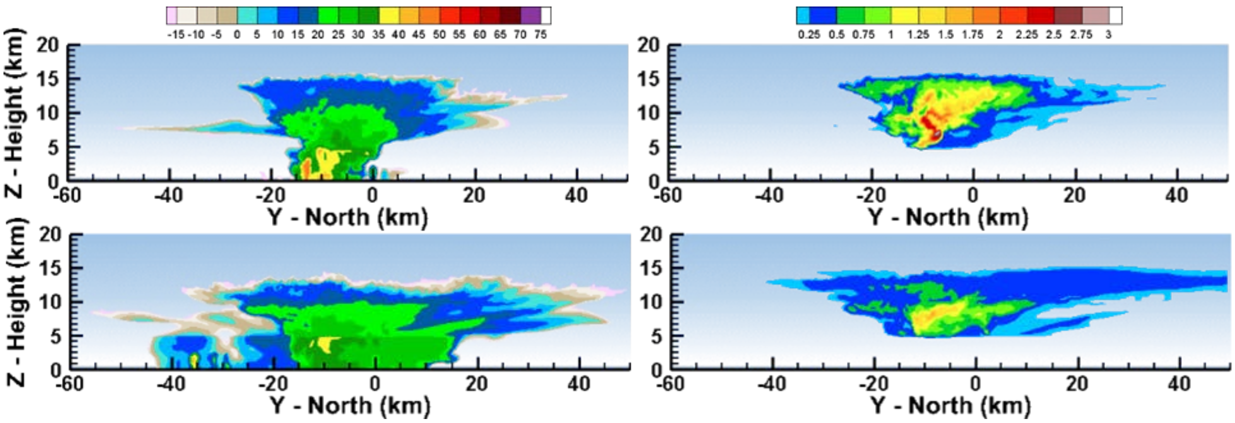

Figure 8. Vertical cross section orthogonal to convective line for radar reflectivity factor (dBZ) and ice water content. Top row at t = 165 min during intense stage, bottom row at t = 232.5 min during decay stage. Left column is radar reflectivity factor with the contours replicating the standard NEXRAD color pattern (above column), and the right column is the ice water concentration with the contour map above the column.

B. Analysis of Mature Stage

A comparison of the simulated ice water field with other simulated fields is shown in Figs. 9-12 for the mature convective system. The horizontal cross sections again are taken at z = 10 km, near flight level. Note that IWC in excess of 0.5 $g\ m^{-3}$ are nearly continuous along a line at y = -10 km, which is parallel to and just behind the front edge of the convective system. Ice water concentrations greater than 1 $g\ m^{-3}$ extend approximately 40 km downshear (northwest) of the location where peak values exceed 2.5 $g\ m^{-3}$. As shown in Fig. 9, the radar reflectivity factor is mostly between 10 dBZ - 23 dBZ. Small areas of green (23 dBZ - 33 dBZ) are located within the regions of highest IWC. From these results, it would appear difficult to avoid regions of HIWC if the only available guide was the radar reflectivity factor at flight level.

The coldest tops (Fig. 10) have coalesced by this time and have expanded downshear beyond the model's lateral boundary. Some upstream expansion of the cloud tops can be noted as well. The coldest (and highest) tops at this time are displaced downshear from the regions of significant ice water concentration. A comparison of Figs. 9 and 10 show that the cold cloud-top signatures are much larger than the regions with either significant radar reflectivity factor or ice water content during this stage of development.

Simulated turbulence at flight levels are very light for the mature system (Fig. 11). The root-mean-square (rms) values of normal g-load are processed from TASS output according to methods described in references [17,39]. Since peak g-accelerations are about a factor of three or four greater than rms-g values,[40] the peak g-accelerations estimated from Fig. 11 are less than 0.5 g. The absence of strong turbulence is consistent with pilot briefings from actual HIWC incidents.[9] Flights through HIWC conditions during NASA's 2015 DC-8 HIWC campaign encountered turbulence ranging from light to nonexistent.

The standard deviation (sigma) of the horizontal velocity component orthogonal to the convective line is shown in Fig. 12. The sigma values are several $m\ s^{-1}$ or less, and are greatest in the areas with larger IWC.

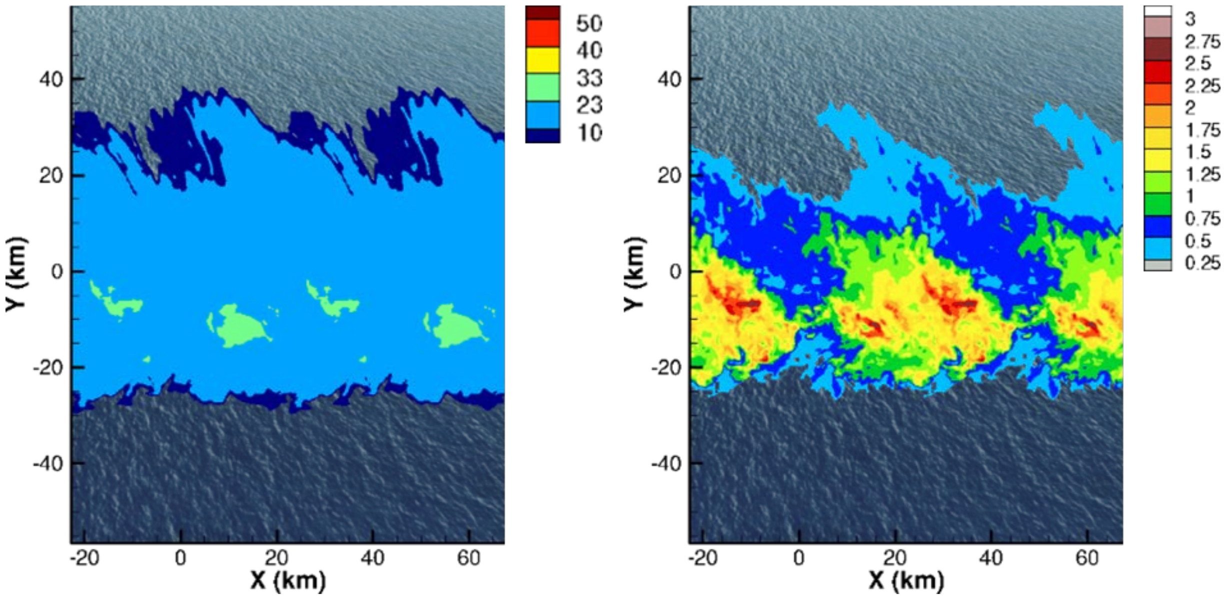

Figure 9. Comparison of simulated radar reflectivity factor (left) with ice water concentration (right) at 10 km elevation for mature system (t = 210 min). Radar reflectivity factor is in dBZ and IWC is in g m^{-3}.

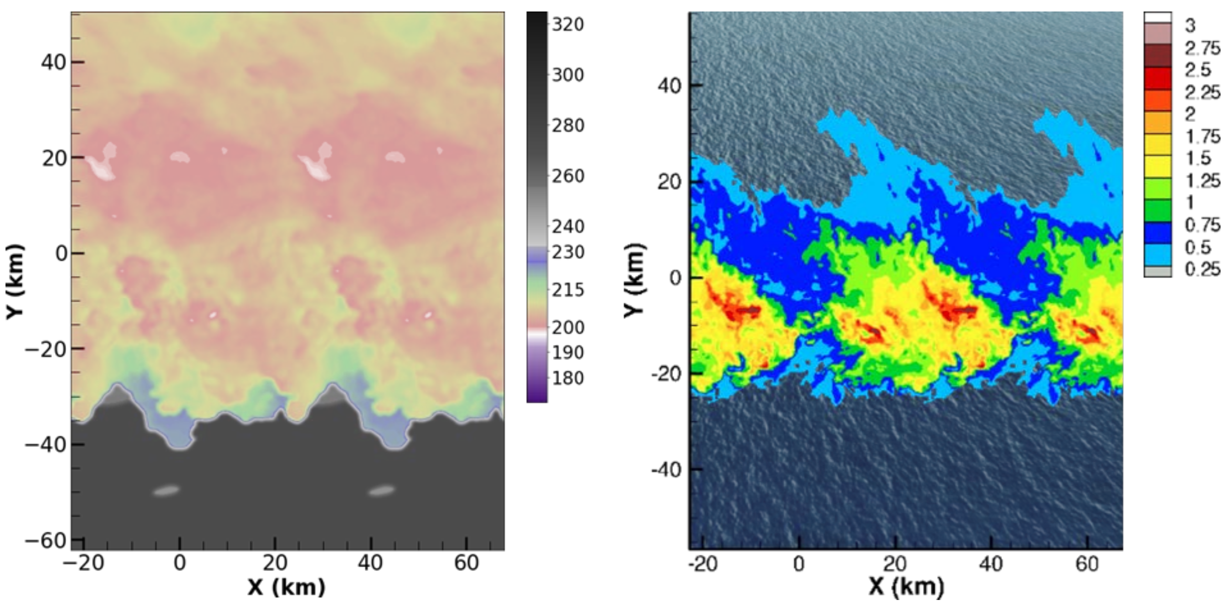

Figure 10. Same as in Fig. 9, but left figure is cloud top temperature in degrees Kelvin.

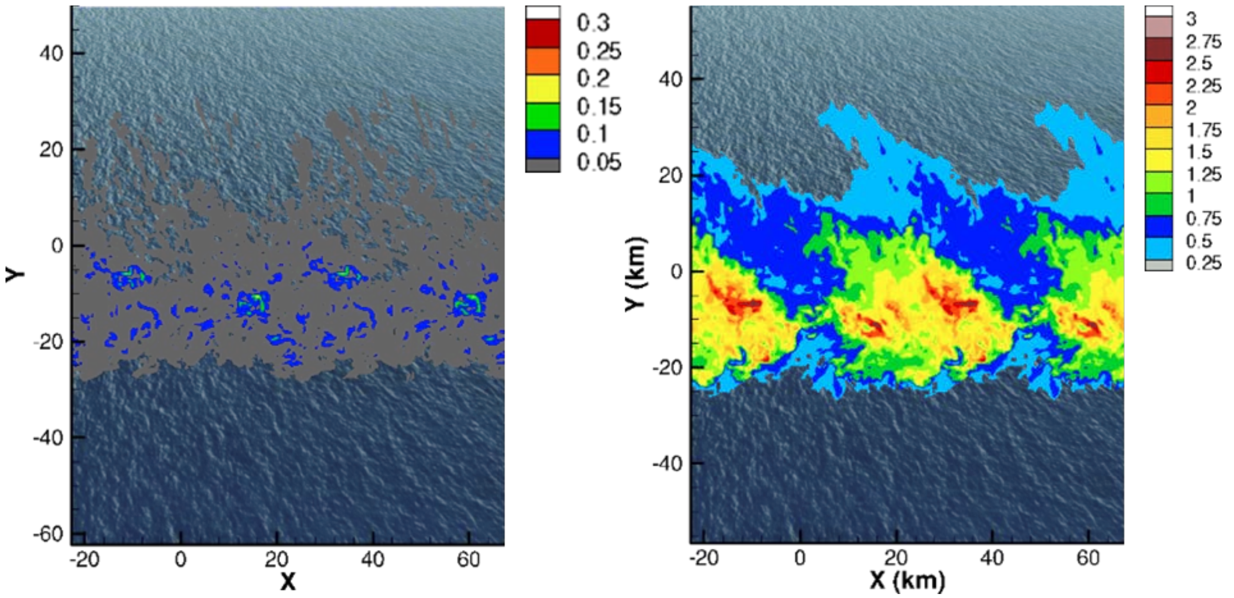

Figure 11. Comparison of simulated turbulence intensity (left) assuming a B-757, and ice water concentration (right). Both plots are at 10 km elevation for mature system (t = 210 min). Turbulence intensity expressed in RMS-g accelerations and IWC is in g m^{-3}.

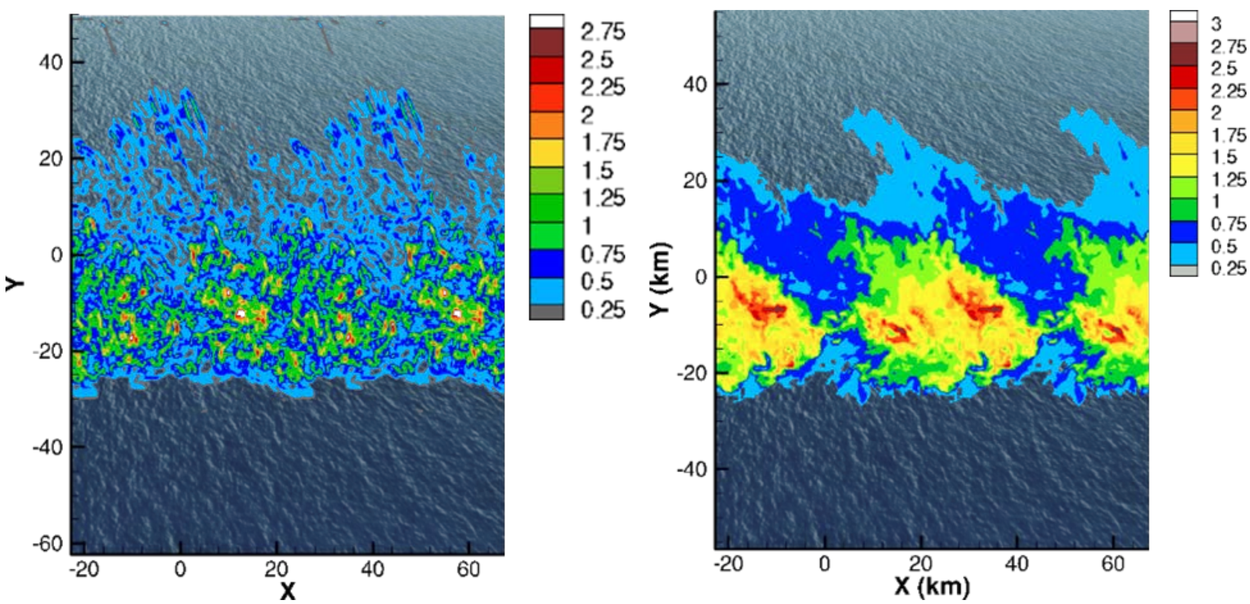

Figure 12. Same as in Fig. 11, but left figure is sigma-V. The standard deviation is computed assuming a one km moving box. Units for sigma V are in m/s, and IWC is in g m^{-3}.

VI. Summary and Discussion

A mesoscale convective line is simulated using the TASS model. The case represents a system that was observed during the HAIC-HIWC 2014 field campaign in Darwin, Australia. The simulated mesoscale convective system has high ice water concentrations for sustained periods, as confirmed from observations of a research aircraft. Many of the features that were observed and are known to occur from HIWC incidents are captured in the simulation of this event. From these results, it would appear difficult to avoid regions of HIWC if the only available guide is the radar reflectivity factor at flight level.

Analysis of the simulation indicated that the long-lived system was maintained by an ensemble of pulsing convective plumes, which supply high concentrations of ice crystals to a growing cloud canopy. Many of these plumes originated along the forward (southeastern) edge of the system, but some formed underneath the canopy near the back end. There was no evidence of an organized, continuous, and quasi-steady updraft structure that acted to maintain the convective system.

At flight level, ice water concentrations exceeding 2 $g\ m^{-3}$ persisted beyond the most intense stages of the convective system. The highest ice water concentrations correlated with the locations of the coldest tops and peak radar reflectivity during the early period of the storm system. As the system matured, substantial areas of HIWC extended downstream from locations with the highest radar reflectivity. During the decay stage of the convective system, the coldest tops began to warm and were displaced downshear from the highest regions of ice water content.

The modeled mesoscale convective system has a structure very similar to that described and conceptualized by Houze et al.,[8, 41] as shown in Fig. 14. From guidance provided by our case simulation, an expected region for high ice water concentrations is added to their conceptual model as depicted by the yellow shaded region.

The modeling results were achieved without tuning parameters specifically for application to HIWC type cases. The TASS model can be robustly applied to other types of convection as well.

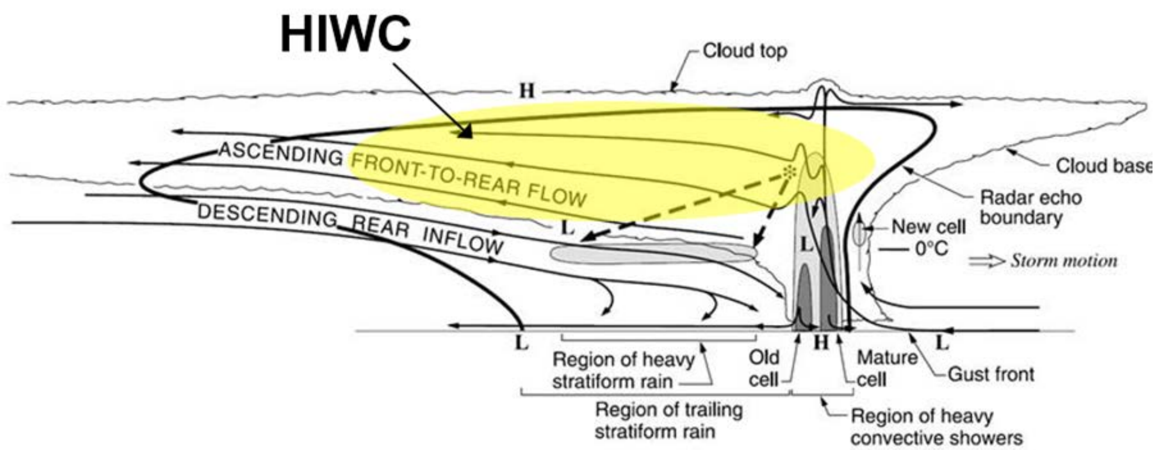

Figure 13. Conceptual model of a convective line with trailing-stratiform precipitation viewed in a vertical cross section oriented perpendicular to the line. Intermediate and strong radar reflectivity is indicated by medium and dark shading, respectively. Dashed-line arrows indicate fallout trajectories of ice particles passing through the melting layer. HIWC denoted by yellow shading. [Adapted from Houze et al. 1989 ©American Meteorological Society. Used with permission.].[8, 41]

References

[1]Mason, J.G., Strapp, J.W., and Chow, P., "The Ice Particle Threat to Engines in Flight," AIAA 2006-206, doi:10.2514/6.2006206.

[2]Lawson, R.P., Augus, L.J., and Heymsfield, A.J., "Cloud Particle Measurements in Thunderstorm Anvils and Possible Weather Threat to Aviation," *Journal of Aircraft*, Vol. *35*, No. 1, January-February 1998, pp. 113-121, doi: 10.2514/2.2268.

[3]Addy, H.E., Jr., and Veres, J.P., "An Overview of NASA Engine Ice-Crystal Icing," SAE International, 2011-38-0017, doi:10.4271/2011-38-0017.

[4]Grandin, A., Merle, J-M., Weber, M., Strapp, J.W., Protat, A., and King, P. "AIRBUS Flight Tests in High Ice Water Content Regions," AIAA 2014-2753, doi:10.2514/6.2014-2753.

[5]Protat, A., and Rauniyar, S., Kumar, V.V., and Strapp, J.W., "Optimizing the Probability of Flying in High Ice Water Content Conditions in the Tropics Using a Regional-Scale Climatology of Convective Cell Properties," *Journal of Applied Meteorology and Climatology*, Vol. 53, November 2014, pp. 2438-2456, doi:10.1175/jamc-d-14-0002.1.

[6]Dezitter, F., Grandin, A., Brenguier, J.L., Hervy, F., Schlager, H., Villedieu, P., and Zalamansky, G., "HAIC (High Altitude Ice Crystals)," AIAA 2013-2674, doi:10.2514/6.2013-2674.

[7]Bravin, M., and Strapp, J., "A Continuing Investigation of Diurnal and Location Trends in an Ice Crystal Icing Engine Event Database," *SAE Int. J. Adv. & Curr. Prac. In Mobility 2(1)*, 2020, pp. 90-105, https://doi.org/10.4271/2019-01-1964.

[8]Houze, R.A., Jr., "Mesoscale Convective Systems," *Review of Geophysics*, Vol. 42, RG4003, 2004, pp. 1-43, doi:10.1029/2004RG000150.

[9]Grzych, M.L., and Mason, J.G., "Weather Conditions Associated with Jet Engine Power Loss and Damage due to Ingestion of Ice Particles: What we've Learned Through 2009," 14th Conference on Aviation, Range, and Aerospace Meteorology, American Meteorological Society, Paper Number 6.8, January 2010, paper_165923.

[10]Mason, J.G., and Grzych, M., "The Challenges Identifying Weather Associated with Jet Engine Ice Crystal Icing," SAE International 2011-38-0094, doi:10.4271/2011-38-0094.

[11]Ratvasky, T.P., Harrah, S.D., Strapp, J., Lille, L.E., Proctor, F.H., Strickland, J.K., Hunt, P.J., Bedka, K., Diskin, G., Nowak, J.B., Bui, T.P., Bansemer, A., and Dumont, C., "Summary of the High Ice Water Content (HIWC) RADAR Flight Campaigns," SAE International, doi: 10.4271/2019-01-2027.

[12]Anonymous, "High Altitude Ice Crystals," URL: https://cordis.europa.eu/project/id/314314, accessed Nov 2020.

[13]Anonymous, "Final Report Summary – HAIC (High Altitude Ice Crystals)," URL: https://cordis.europa.eu/project/id/314314/reporting, accessed Nov 2020.

[14] Strapp, J.W., Lilie, L.E., Ratvasky, T.P., Davison, C., and Dumont, C., "Isokinetic TWC Evaporator Probe: Development of the IKP2 and Performance Testing for the HAIC-HIWC Darwin 2014 and Cayenne-2015 Field Campaigns," AIAA 2016-4059, doi:10.2514/6.2016-4059.

[15]Proctor, F.H., "The Terminal Area Simulation System, Volume I: Theoretical Formulation," April 1987, NASA CR-4046.

[16]Proctor, F. H., and Bowles, R.L., "Three-Dimensional Simulation of the Denver 11 July 1988 Microburst-Producing Storm," *Meteorology and Atmospheric Physics*, Vol. 49, 1992, pp. 107-124, doi:10.1007/bf01025403.

[17]Proctor, F.H., Hamilton, D.W., and Bowles, R.L., "Numerical Study of a Convective Turbulence Encounter," AIAA 2002-0944, doi:10.2514/6.2002-944.

[18]Ahmad, N., and Proctor, F.H., "Simulation of Benchmark Cases with the Terminal Area Simulation System," AIAA 2011-1005, doi:10.2514/6.2011-1005.

[19]Proctor, F.H., Ahmad, N.N., and Limon Duparcmeur, F.M., "Numerical Simulation of a Tornado Generating Supercell," AIAA 3012-0557, doi:10.2514/6.2012-557.

[20]Lin, Y-L., Farley, R.D., and Orville, H.D., "Bulk Parameterizations of the Snow Field in a Cloud Model," *Journal of Climate and Applied. Meteorology*, Vol. 32, 1983, pp. 1065-1092, doi:10.1175/1520-0450(1983)022%3C1065:bpotsf%3E2.0.co;2.

[21]Rutledge, S.A., and Hobbs, P.V., "The Mesoscale and Microscale Structure and Organization of Clouds and Precipitation. VIII: A Model for the "Seeder-Feeder" Process in Frontal Rainbands," *Journal of the Atmospheric Science*, Vol. 40, May, 1983, pp. 1185-1206, doi:10.1175/1520-0469(1983)040%3C1185:tmamsa%3E2.0.co;2.

[22]Berry, E.X., and Reinhardt, R.E., "An Analysis of Cloud Drop Growth by Collection. Part I: Double Distributions," *Journal of the. Atmospheric Science*, Vol. 31, October 1974, pp. 1814-1824, doi:10.1175/1520-0469(1974)031%3C1814:aaocdg%3E2.0.co;2.

[23]Berry, E.X., and Reinhardt, R.E., "An Analysis of Cloud Drop Growth by Collection. Part II: Single Initial Distributions," *Journal of the. Atmospheric Science*, Vol. 31, October 1974, pp. 1825-1831, doi:10.1175/1520-0469(1974)031%3C1825:aaocdg%3E2.0.co;2.

[24]Proctor, F.H., 1989, "Numerical Simulations of an Isolated Microburst. Part II: Sensitivity Experiments," *Journal of the Atmospheric Science*, Vol. 46, 15 July 1989, pp. 2143-2165, doi:10.1175/1520-0469(1989)046%3C2143:nsoaim%3E2.0.co;2.

[25]Woods, C.P., Stoelinga, M.T., and Locatelli, J.D., "Size Spectra of Snow Particles Measured in Wintertime Precipitation in the Pacific Northwest," J*ournal of the Atmospheric Science*, Vol. 65, January 2008, pp. 189- 205, doi:10.1175/2007jas2243.1.

[26]Smith, P.L., Jr., Myers, C.G., and Orville, H.D., "Radar Reflectivity Factor Calculations in Numerical Cloud Models using Bulk Parameterizations of Precipitation," *Journal of Applied Meteorology*, Vol. 14, September 1975, pp. 1156-1165, doi:10.1175/1520-0450(1975)014%3C1156:rrfcin%3E2.0.co;2.

[27]Proctor, F.H., "Numerical Simulation of Wake Vortices Measured During the Idaho Falls and Memphis Field Programs," 14th AIAA Applied Aerodynamic Conference, Proceedings, Part II, June 1996, AIAA 96-2496-CP, pp. 943-960, doi:10.2514/6.1996-2496.

[28]Leonard, B.P., MacVean, M.K., and Lock, A.P., "The Flux-Integral Method for Multidimensional Convection and Diffusion," *Applied Mathematical Modeling*, Vol. 19, 1995, pp. 333-342, doi:10.1016/0307-904x(95)00017-e.

[29]van Leer, B., "Towards the Ultimate Conservative Difference Scheme: V, A Second-Order Sequel to Godunov's Method," *Journal of Computational Physics*, Vol. 32, 1979, pp. 101-136, doi:10.1016/0021-9991(79)90145-1.

[30]Ahmad, N.N., and Proctor, F.H., "Advection of Microphysical Scalars in Terminal Area Simulation System (TASS)," AIAA 2011-1004, doi:10.2514/6.2011-1004.

[31]Klemp, J. B., and Wilhelmson, R., "The Simulation of Three-Dimensional Convective Storm Dynamics," *Journal of the Atmospheric Sciences*, Vol. 35, June 1978, pp. 1070-1096, doi:10.1175/1520-0469(1978)035%3C1070:tsotdc%3E2.0.co;2.

[32]Switzer, G.F., "Validation Tests of TASS for Application to 3-D Vortex Simulations," October 1996, NASA CR-4756.

[33]Han, J., Lin, Y.-L., Schowalter, D. G., Arya, S. P., and Proctor, F. H., "Large Eddy Simulation of Aircraft Wake Vortices within Homogeneous Turbulence: Crow Instability," *AIAA Journal*, Vol. 38, February 2000, pp 292-300, doi:10.2514/2.956.

[34]Proctor, F.H., "Interaction of Aircraft Wakes from Laterally Spaced Aircraft," AIAA 2009-0343, doi:10.2514/6.2009-343.

[35]Switzer, G. and Proctor, F., "Terminal Area Simulation System User's Guide – Version 10.0," January 2014, NASA TM-2014-218150.

[36]May, R. M., Arms, S. C., Marsh, P., Bruning, E. and Leeman, J. R., "MetPy: A Python Package for Meteorological Data", doi:10.5065/D6WW7G29

[37]Harrah, S.D., Strickland, J.K., Hunt, P.J., Proctor, F.H., Switzer, G.F., Ratvasky, T.P., Strapp, J.W., Lilie, L., and Dumont, C., "Radar Detection of High Concentrations of Ice Particles – Methodology and Preliminary Flight Tests," SAE International, doi: 10.4271/2019-01-2028.

[38]Heymsfield, G.M., Tian, L., Heymsfield, A.J., Li, L., and Guimond, S., "Characteristics of Deep Tropical and Subtropical Convection from Nadir-Viewing High Altitude Airborne Radar," J*ournal of the Atmospheric Science*, Vol. 67, February 2010, pp. 285-308, doi:10.1175/2009jas3132.1.

[39]Ahmad, N.N., and Proctor, F.H., "Large Eddy Simulations of Severe Convection Induced Turbulence," AIAA 2011-3201, doi:10.2514/6.2011-3201.

[40]Hamilton, D.W., Proctor, F.H., and Ahmad, N.N., "Flight Tests of the Turbulence Prediction and Warning System (TPAWS)," February 2012, NASA TM-2012-217337.

[41]Houze, R.A., Jr., Rutledge, S.A., Biggerstaff, M.I., and Smull, B.F., "Interpretation of Doppler Weather Radar Displays of Midlatitude Mesoscale Convective Systems," *Bulletin of the American Meteorological Society*, Vol. 70, No. 6, June 1989, pp. 608-619, doi:10.1175/1520-0477(1989)070%3C0608:iodwrd%3E2.0.co;2.

REPORT DOCUMENTATION PAGE	*Form Approved OMB No. 0704-0188*

1. REPORT DATE *(DD-MM-YYYY)*	**2. REPORT TYPE**	**3. DATES COVERED** *(From - To)*
1-11-2020	Technical Memorandum	

4. TITLE AND SUBTITLE	**5a. CONTRACT NUMBER**
High Ice Water Content Associated with a Darwin, Australia, Mesoscale Convective System	80LARC17C0003
	5b. GRANT NUMBER
	5c. PROGRAM ELEMENT NUMBER
6. AUTHOR(S)	**5d. PROJECT NUMBER**
Fred H. Proctor Distinguished Research Associate Langley Research Center, Hampton, Virginia George F. Switzer Analytical Mechanics Associates, Inc., Hampton, Virginia	**5e. TASK NUMBER**
	5f. WORK UNIT NUMBER

7. PERFORMING ORGANIZATION NAME(S) AND ADDRESS(ES)	**8. PERFORMING ORGANIZATION REPORT NUMBER**
NASA Langley Research Center Hampton, VA 23681-2199	
9. SPONSORING/MONITORING AGENCY NAME(S) AND ADDRESS(ES)	**10. SPONSOR/MONITOR'S ACRONYM(S)**
National Aeronautics and Space Administration Washington, DC 20546-0001	NASA
	11. SPONSOR/MONITOR'S REPORT NUMBER(S)
	NASA-TM-20205010032

12. DISTRIBUTION/AVAILABILITY STATEMENT

Unclassified
Subject Category
Availability: NASA STI Program (757) 864-9658

13. SUPPLEMENTARY NOTES

14. ABSTRACT

A mesoscale convective complex that occurred during the 2014 Darwin, Australia, flight campaign is examined via a three-dimensional, numerical simulation. The focus of the study is to better understand the presence and development of High Ice Water Content (HIWC) that was observed in the actual storm. Although peak values of ice water content may occur early in the storm lifetime, large areas of high concentrations expand with time and persist even when the storm tops begin to warm. The storm canopy which contains HIWC, has low radar reflectivity factor and is fed by an ensemble of regenerating thermal plumes. Detection via weather radar of the aviation hazard associated HIWC is challenging due the low values of radar reflectivity factor.

15. SUBJECT TERMS

Aviation hazards, high ice water concentrations, mesoscale convective system, numerical weather models, microphysics, radar meteorology, airborne weather radar, numerical cloud model, thunderstorms, convective dynamics, icing

16. SECURITY CLASSIFICATION OF:			**17. LIMITATION OF ABSTRACT**	**18. NUMBER OF PAGES**	**19a. NAME OF RESPONSIBLE PERSON**
a. REPORT	**b. ABSTRACT**	**c. THIS PAGE**			STI Help Desk (email: help@sti.nasa.gov)
					19b. TELEPHONE NUMBER *(Include area code)*
U	U	U	UU	22	(757) 864-9658